

# SGAD: Semantic and Geometric-aware Descriptor for Local Feature Matching

Xiangzeng Liu<sup>1\*</sup>, Chi Wang<sup>1\*†</sup>, Guanglu Shi<sup>1</sup>, Xiaodong Zhang<sup>1</sup>, Qiguang Miao<sup>1†</sup>, Miao Fan<sup>2</sup>

<sup>1</sup>Xidian University <sup>2</sup>Navinfo Europe B.V

Project page: <https://mr-chiwang.github.io/SGAD/>

## Abstract

Local feature matching remains a fundamental challenge in computer vision. Recent Area to Point Matching (A2PM) methods have improved matching accuracy. However, existing research based on this framework relies on inefficient pixel-level comparisons and complex graph matching that limit scalability. In this work, we introduce the Semantic and Geometric-aware Descriptor Network (SGAD), which fundamentally re-thinks area-based matching by generating highly discriminative area descriptors that enable direct matching without complex graph optimization. This approach significantly improves both accuracy and efficiency of area matching. We further improve the performance of area matching through a novel supervision strategy that decomposes the area matching task into classification and ranking subtasks. Finally, we introduce the Hierarchical Containment Redundancy Filter (HCRF) to eliminate overlapping areas by analyzing containment graphs. SGAD demonstrates remarkable performance gains, reducing runtime by  $60\times$  (0.82s vs. 60.23s) compared to MESA. Extensive evaluations show consistent improvements across multiple point matchers: SGAD+LoFTR reduces runtime compared to DKM, while achieving higher accuracy (0.82s vs. 1.51s, 65.98 vs. 61.11) in outdoor pose estimation, and SGAD+ROMA delivers +7.39% AUC@5° in indoor pose estimation, establishing a new state-of-the-art.

## 1. Introduction

Feature matching establishes precise pixel-level correspondences between images, which is fundamental to numerous computer vision tasks, including SFM [30], SLAM [3], visual localization [28, 29], and image re-

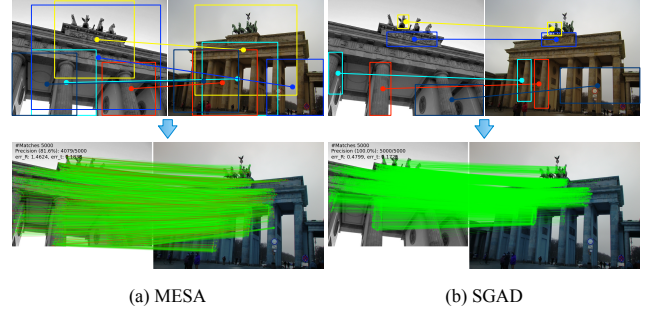


Figure 1. Area matching comparison between MESA and our proposed SGAD. SGAD accurately identifies highly coherent corresponding areas, establishing a stronger foundation for subsequent pixel-level matching.

trieval [24]. Nevertheless, achieving accurate pixel correspondences remains challenging due to scale variations, viewpoint changes, illumination differences, and repetitive patterns.

Most existing methods process entire image pairs through extensive pixel comparisons, increasing computational complexity and often leading to mismatches due to the involvement of many non-correlated pixels. Recent research has addressed this by identifying overlapping areas in advance and restricting matching to those areas. Approaches such as [6, 14] segment overlapping areas before matching, though implicit learning introduces non-reusable computational overhead. TopicFM [12] classifies pixels into topics, limiting matching to pixels within the same topic. SGAM [40] introduced the Area to Point Matching (A2PM) framework, improving correspondence accuracy by matching semantic areas before point matching, yet its implementation relies on explicit semantic labels, making it vulnerable to annotation inaccuracies.

MESA [39] addresses the dependency on semantic labels by incorporating the Segment Anything Model (SAM) [15]. However, it suffers from two critical limitations: high computational cost due to inefficient pixel-

\*Equal Contribution. †Corresponding Author.

level comparisons and complex graph matching, and reduced accuracy from non-overlapping areas introduced by its merging strategy. Similarly, DMESA [38] enhances matching efficiency by generating a dense matching distribution, yet still struggles with the computational burden of graph matching and area merging limitations of MESA. As shown in Fig. 1(a), MESA’s area correspondences can suffer from content inconsistencies, which hinders subsequent refinement.

To overcome these fundamental limitations, we propose a novel paradigm: the Semantic and Geometric-aware Descriptor Network (SGAD). Our approach generates highly discriminative area descriptors that enable straightforward matching with a simple descriptor matcher, eliminating the need for complex graph optimization. This approach is significantly more efficient and scalable. Specifically, SGAD first segments images into areas using SAM [15] and then extracts initial semantic features for each area via DINOv2 [23], providing rich contextual information about the area content. To address the lack of spatial context in these features, a geometric positional encoding module embeds spatial relationship information, reducing interference from visually similar areas at different positions. Subsequently, alternating self-attention and cross-attention mechanisms [35] model complex relationships between areas both within and across images. Additionally, our Hierarchical Containment Redundancy Filter (HCRF) constructs containment relations graphs and filters out redundant areas based on node relationships. For training, we introduce a novel dual-task supervision strategy that decomposes area matching into classification and ranking. This joint optimization enables the model to learn both absolute (classification) and relative (ranking) similarity patterns. As shown in Fig. 1(b), SGAD produces more content-consistent area matching results than MESA, providing a stronger foundation for subsequent fine-grained pixel-level matching.

The key contributions of our work are as follows:

- 1) A novel area matching paradigm (SGAD) that achieves efficient and accurate area matching, addressing the efficiency and scalability limitations of prior A2PM frameworks (Secs. 3.1 and 3.2).
- 2) A dual task learning framework decomposing area matching into classification and ranking subtasks, jointly optimizing both absolute and relative similarity patterns (Sec. 3.4, validated in Tab. 6).
- 3) Consistent performance improvements across multiple point matchers on indoor and outdoor datasets. SGAD+LoFTR (semi-dense) outperforms DKM (dense) in both efficiency and accuracy on MegaDepth (0.82s *vs.* 1.51s, 65.98 *vs.* 61.11). Fur-

thermore, our method establishes a new state-of-the-art when integrated with ROMA.

## 2. Related Work

**Classic Feature Matching.** Feature matching methods can be broadly classified into detector-based and detector-free approaches. Detector-based methods follow a three-stage pipeline: feature detection [2, 8, 20], description [9, 25], and matching [18, 27, 37]. While feature detection reduces the search space, these methods struggle with large viewpoint changes and textureless scenes. In contrast, detector-free methods [10–12, 31] enhance keypoint repeatability by directly extracting dense visual descriptors and generating dense matches. However, the large-scale dense comparisons incur significant computational overhead, and often lead to a higher rate of false matches.

**Multi-stage Feature Matching.** To reduce redundant matches, researchers have explored various strategies. Methods like [22, 41] adopted uniform patch division but overlooked image semantic structure. TopicFM [12] addressed this by introducing a topic model-based pixel classification method, though its generalizability and cross-image consistency remain limited. These approaches highlight the value of semantics, but its potential remains largely underutilized for efficient and accurate matching.

**Area to Point Matching Methods.** The A2PM framework, introduced by SGAM [40], enhances performance by restricting point matching to semantically matched areas. However, SGAM heavily relies on pre-defined semantic labels, making it sensitive to annotation quality. MESA [39] mitigated this dependency by leveraging the SAM [15], but introduced new challenges: dense activity map computation and complex graph-matching optimization created substantial computational overhead, while area merging often introduced non-overlapping areas into the initial segmentation, degrading matching quality. Although DMESA improved efficiency through dense matching distributions, it still inherits the fundamental limitations of graph-matching and area merging from MESA.

Our method fundamentally differs from previous approaches by rethinking area-based matching through a dedicated descriptor network. Prior work often relies on complex matching algorithms to compensate for inadequate area representations. In contrast, SGAD focuses on generating highly discriminative descriptors from the outset. This enables straightforward matching without complex graph optimization. This paradigm shift significantly improves both matching accuracy and computational efficiency, addressing the core limitations of existing A2PM approaches.

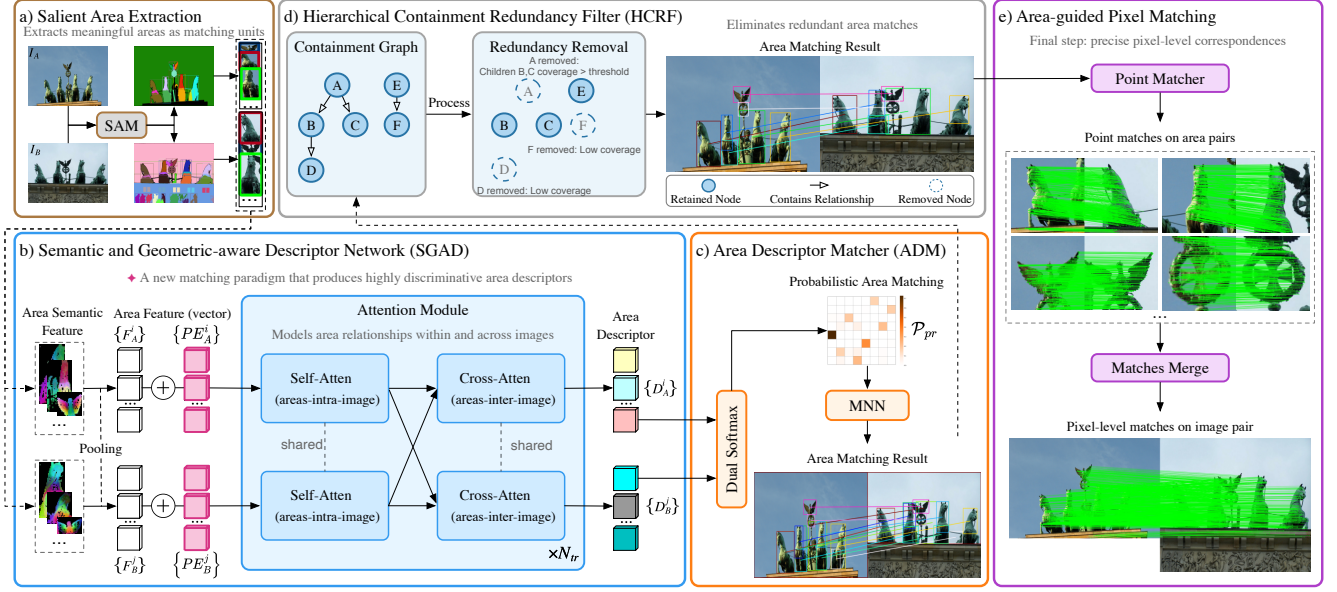


Figure 2. Overview of the SGAD method. SGAD consists of five components: (a) Salient areas are extracted from image pairs using SAM. (b) Semantic features are extracted by DINOv2 and average-pooled into vectors  $\{F_A^i\}$  and  $\{F_B^j\}$ . Spatial relationships are encoded through geometric positional embeddings  $\{PE_A^i\}$  and  $\{PE_B^j\}$ . Alternating self-attention and cross-attention model complex relationships between areas both within and across images, producing final descriptors  $\{D_A^i\}$  and  $\{D_B^j\}$ . (c) Dual-softmax estimation is applied to compute the area matching probability matrix  $\mathcal{P}_{pr}$ , with the Mutual Nearest Neighbor (MNN) algorithm selecting matched pairs  $\mathcal{M}$ . (d) Hierarchical Containment Redundancy Filter (HCRF) removes nested areas from  $\mathcal{M}$ , retaining non-redundant matched pairs. (e) Local feature matching is performed within selected matched area pairs, with final pixel-level matching obtained by aggregating all matched points across areas.

### 3. Method

Fig. 2 illustrates the architecture of our proposed Semantic and Geometric-aware Descriptor Network (SGAD). SGAD first establishes matches between salient areas and then guides precise pixel-level matching within these areas. The framework consists of five key components: (a) salient area extraction, (b) area description through our semantic and geometric-aware descriptor network, (c) area matching with a simple descriptor matcher, (d) hierarchical containment redundancy filter, and (e) guided point matching within matched areas.

#### 3.1. Salient Area Extraction and Description

**Area Feature Extraction.** We leverage SAM to generate instance masks for  $I_A$  and  $I_B$ , identifying the minimum bounding rectangles of these masks as extracted areas, forming sets  $R_A = \{R_A^i \mid i = 1, 2, \dots, m\}$  and  $R_B = \{R_B^j \mid j = 1, 2, \dots, n\}$  as illustrated in Fig. 2(a). The indices  $i$  and  $j$  used later will follow these same ranges. Next, we use a frozen DINOv2 encoder to extract semantically rich features for each area, which are then average-pooled to obtain feature vectors  $\{F_A^i\}$  and  $\{F_B^j\}$ , significantly reducing

input length for subsequent attention operations.

**Geometric Positional Encoding.** Although  $\{F_A^i\}$  and  $\{F_B^j\}$  capture strong semantic features, they lack global spatial information, as each feature is extracted independently. Such global spatial context is crucial for accurate area matching. To address this, we designed a geometric positional encoding module based on relative geometric attributes between areas. Given the two sets of areas,  $\{R_A^i\}$  and  $\{R_B^j\}$ , with center coordinates  $(x_A^i, y_A^i)$  and  $(x_B^j, y_B^j)$ , we compute the geometric spatial attributes of each area relative to all other areas within the same image, including the Euclidean distances and relative angles between them.

The Euclidean distance is given by:

$$\begin{cases} d_A^{il} = \sqrt{(x_A^i - x_A^l)^2 + (y_A^i - y_A^l)^2} \\ d_B^{jk} = \sqrt{(x_B^j - x_B^k)^2 + (y_B^j - y_B^k)^2}, \end{cases} \quad (1)$$

where  $l$  and  $k$  are the intra-image area indices for Image A and Image B, respectively.

The relative angle is computed using the arctangent:

$$\begin{cases} \theta_A^{il} = \text{atan2}(y_A^i - y_A^l, x_A^i - x_A^l) \\ \theta_B^{jk} = \text{atan2}(y_B^j - y_B^k, x_B^j - x_B^k). \end{cases} \quad (2)$$

The positional embedding for each area is then generated by an MLP. Its input is the average of the geometric vectors,  $[d^{il}, \sin(\theta^{il}), \cos(\theta^{il})]$ , computed pairwise with all other areas in the same image:

$$\begin{cases} PE_A^i = \text{MLP} \left( \frac{1}{m-1} \sum_{l \neq i}^m [d_A^{il}, \sin(\theta_A^{il}), \cos(\theta_A^{il})] \right) \\ PE_B^j = \text{MLP} \left( \frac{1}{n-1} \sum_{k \neq j}^n [d_B^{jk}, \sin(\theta_B^{jk}), \cos(\theta_B^{jk})] \right). \end{cases} \quad (3)$$

Then, these positional embeddings are added to the area features:

$$\begin{cases} \hat{F}_A^i = F_A^i + PE_A^i \\ \hat{F}_B^j = F_B^j + PE_B^j. \end{cases} \quad (4)$$

This approach enhances spatial representation by integrating relative positions and geometric relationships.

**Attention Module.** To model complex relationships between areas both within and across images, we adopt an attention mechanism enabling both intra-image and inter-image information interaction. For the area feature sequences  $\{\hat{F}_A^i\} = [\hat{F}_A^1, \hat{F}_A^2, \dots, \hat{F}_A^m]$  and  $\{\hat{F}_B^j\} = [\hat{F}_B^1, \hat{F}_B^2, \dots, \hat{F}_B^n]$ , we first apply self-attention separately within  $\{\hat{F}_A^i\}$  and  $\{\hat{F}_B^j\}$ , followed by cross-attention between them. By stacking  $N_{tr}$  layers of alternating self-attention and cross-attention, we obtain final area descriptors  $\{D_A^i\}$  and  $\{D_B^j\}$  with improved expressiveness and discriminative power of each area feature.

### 3.2. Area Descriptor Matcher

**Matching Probabilities Estimation.** We compute the score matrix  $\mathcal{S}$  between the area descriptors:

$$\mathcal{S}(i, j) = \frac{1}{\tau} \cdot \langle D_A^i, D_B^j \rangle, \quad (5)$$

where  $\tau$  is a temperature parameter adjusting score sharpness.

Dual-softmax [26, 34] estimates the probability matrix for matching area descriptors. The matching probability  $\mathcal{P}_{pr}$  for a pair  $(i, j)$  is:

$$\mathcal{P}_{pr}(i, j) = \text{softmax}(\mathcal{S}(i, \cdot))_j \cdot \text{softmax}(\mathcal{S}(\cdot, j))_i. \quad (6)$$

**Match Selection.** Based on confidence matrix  $\mathcal{P}_{pr}$ , we select matches with confidence values above threshold  $\lambda_{pr}$ . To enforce one-to-one matching and exclude potential outliers, we apply the Mutual Nearest Neighbor (MNN) algorithm to find optimal assignment. The resulting set of area match predictions is:

$$\mathcal{M} = \{(i, j) \mid (i, j) \in \text{MNN}(\mathcal{P}_{pr}), \mathcal{P}_{pr}(i, j) \geq \lambda_{pr}\}. \quad (7)$$

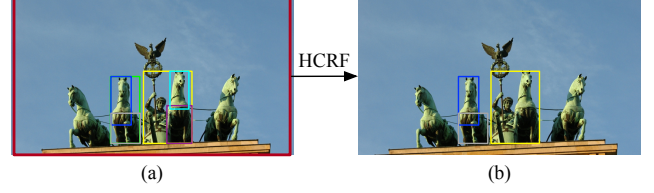


Figure 3. Visualization of the HCRF process. (a) Matching results directly obtained through MNN, with overlapping areas present. (b) Results after filtering through HCRF. HCRF effectively resolves the problem of overlapping areas, preserving the optimal matching results.

### 3.3. Hierarchical Containment Redundancy Filter

Descriptor matching yields matched area pairs as shown in Fig. 2(c). While these pairs accurately identify matching relationships even for multi-level nested areas, extensively overlapping areas introduce significant redundant computations in subsequent point matching (Fig. 3(a)). To address this, we propose a Hierarchical Containment Redundancy Filter (HCRF) to eliminate this redundancy effectively.

We first construct an area containment relationship graph (Fig. 2(d)), representing soft containment controlled by threshold  $\delta_{\text{contain}}$ . The containment relationship is defined as:

$$R_p \text{ contains } R_c \text{ iff } \frac{|R_p \cap R_c|}{|R_c|} \geq \delta_{\text{contain}}, \quad (8)$$

where  $|R_p \cap R_c|$  is the overlapping area and  $|R_c|$  is the size of the contained area.

We traverse the containment graph using Depth-First-Search (DFS) [32] and determine which nodes to retain based on coverage ratio and threshold  $\delta_{\text{cover}}$ . For parent node  $R_p$  and its child nodes  $C(p)$ :

$$\begin{aligned} &\text{If } \frac{|\cup_{c \in C(p)} R_c|}{|R_p|} < \delta_{\text{cover}}, \text{ keep } R_p; \\ &\text{otherwise, keep } \{R_c \mid c \in C(p)\}, \end{aligned} \quad (9)$$

where  $\cup_{c \in C(p)} R_c$  is the union of all child areas and  $|R_p|$  is the parent area size.

We apply this filter on one image (e.g., Image A) and use the resulting indices to prune the match set  $\mathcal{M}$ . The resulting filtered indices identify the most representative area pairs while eliminating redundancy, as shown in Fig. 3(b), significantly improving the efficiency of subsequent point matching.

We deliberately perform filtering after area matching for two key reasons. First, SGAD is highly efficient and completes area matching quickly even without pre-filtering. Second, filtering prematurely could



aggressively prune areas in some cases, reducing the number of matched pairs and thus harming the final point matching performance.

### 3.4. Supervision.

To optimize area matching performance, we design a novel dual-task framework that decomposes the process into classification and ranking subtasks. The classification subtask determines whether area pairs meet basic matching criteria, establishing a foundation for viable matches. The ranking subtask refines this process by selecting the best match from multiple candidates, capturing relative similarity patterns. Through joint optimization with  $\mathcal{L} = \mathcal{L}_{cls} + \mathcal{L}_{rank}$ , our model effectively captures both absolute and relative similarity patterns, ensuring robust matching.

**Area Matching Label.** Following SuperGlue [27], we compute precise pixel-level correspondences using camera poses and depth maps. The ground-truth matching score  $\mathcal{P}_{gt}(i, j)$  is the Intersection over Union (IoU) [36] between area  $R_B^j$  and the projection of area  $R_A^i$  into Image B, denoted as  $\text{proj}(R_A^i)$ , using the ground-truth camera poses:

$$\mathcal{P}_{gt}(i, j) = \frac{|\text{proj}(R_A^i) \cap R_B^j|}{|\text{proj}(R_A^i) \cup R_B^j|}. \quad (10)$$

Area pairs with  $\mathcal{P}_{gt}(i, j)$  above threshold  $\lambda_{gt}$  are considered similar. To create a binary classification ground-truth matrix  $\mathcal{P}_{gt}^{cls}$ , we binarize the confidence matrix  $\mathcal{P}_{gt}$  as:

$$\mathcal{P}_{gt}^{cls}(i, j) = \begin{cases} 1, & \text{if } \mathcal{P}_{gt}(i, j) > \lambda_{gt} \\ 0, & \text{otherwise.} \end{cases} \quad (11)$$

**Classification Supervision.** For the classification task, we employ focal loss [17] with the predicted confidence matrix  $\mathcal{P}_{pr}$  obtained through dual softmax. The classification loss, comprising positive and negative sample components, is defined as:

$$\mathcal{L}_{cls} = -\alpha \cdot (1 - p_t)^\gamma \cdot \log(p_t), \quad (12)$$

where:

$$p_t = \begin{cases} \mathcal{P}_{pr}(i, j) & \text{if } \mathcal{P}_{gt}^{cls}(i, j) = 1 \\ 1 - \mathcal{P}_{pr}(i, j) & \text{if } \mathcal{P}_{gt}^{cls}(i, j) = 0, \end{cases} \quad (13)$$

$\alpha$  controls the weight of positive and negative samples, and  $\gamma$  controls the weight of hard and easy samples.

**Ranking Supervision.** For the ranking task, we adopt ListMLE loss [4]. For each source image area, we extract matching score sequences between this area and all target image areas from both  $\mathcal{P}_{pr}$

and  $\mathcal{P}_{gt}$ , yielding predicted score sequence  $T_{pr} = [T_{pr_1}, T_{pr_2}, \dots, T_{pr_n}]$  and ground-truth score sequence  $T_{gt} = [T_{gt_1}, T_{gt_2}, \dots, T_{gt_n}]$ . Our objective is for  $T_{pr}$  to match the ranking order of  $T_{gt}$ , ensuring matches with higher ground-truth scores receive higher predicted confidence. The ranking loss is defined as:

$$\mathcal{L}_{rank} = -\sum_{k=1}^n \left( T_{pr, \pi_k^*} - \log \sum_{l=k}^n \exp(T_{pr, \pi_l^*}) \right), \quad (14)$$

where  $\pi^*$  represents the permutation of indices that sorts the ground-truth scores  $T_{gt}$  in descending order, and  $T_{pr, \pi_k^*}$  is the predicted score from the sequence  $T_{pr}$  at the  $k$ -th position of this permutation.

## 4. Experiments

### 4.1. Implementation Details

We train separate models for indoor and outdoor environments on the ScanNet [7] and MegaDepth [16] datasets, respectively, with the same training-testing division as in [31]. The model was trained end-to-end using the AdamW [19] optimizer with an initial learning rate of  $1 \times 10^{-4}$  and a batch size of 64. Training time is approximately 2 days on a single RTX A6000 GPU. For feature extraction, we use DINOv2 Large [23] as the backbone.  $N_{tr}$  is set to 4, and the ground-truth matching threshold  $\lambda_{gt}$  is set to 0.2.

### 4.2. Area Matching

For the matching task, we assess performance on the ScanNet1500 [7] and MegaDepth1500 [16] benchmark datasets.

**Experimental setup.** On both indoor and outdoor datasets, we use the Area Under the Curve (AUC) metric to assess performance in correctly identifying matched and non-matched pairs, evaluated across multiple overlap rate thresholds (AUC@0.2, AUC@0.3, AUC@0.4, AUC@0.5). MESA and DMESA do not provide similarity matrices for all regions involved in the matching process, it is not possible to calculate this metric for these methods. Therefore, in addition to quantitative results, we provide qualitative comparisons in Fig. 4.

**Results.** As shown in Tab. 1, SGAD achieves exceptional area matching accuracy, with AUC scores consistently above 95% across all thresholds for both indoor and outdoor environments. Fig. 4 demonstrates that our method achieves more accurate area matching results compared to MESA, particularly in challenging scenarios with large viewpoint changes. This robust matching capability directly contributes to improved results in downstream tasks, as evidenced by subsequent tables (Tabs. 2 to 4).

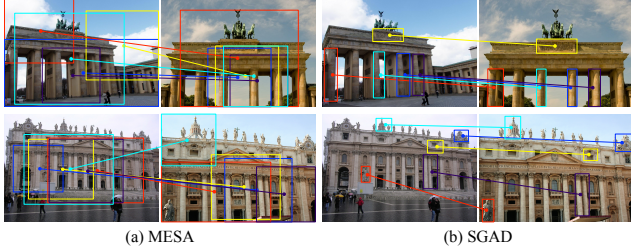


Figure 4. Comparison of area matching results between the proposed method SGAD and MESA. To provide a clear comparison, we randomly selected 5 area pairs for each method.

ScanNet	AUC@0.2 $\uparrow$	AUC@0.3 $\uparrow$	AUC@0.4 $\uparrow$	AUC@0.5 $\uparrow$
SGAD	95.46	96.18	96.78	97.28
MegaDepth	AUC@0.2 $\uparrow$	AUC@0.3 $\uparrow$	AUC@0.4 $\uparrow$	AUC@0.5 $\uparrow$
SGAD	97.39	97.81	98.02	98.18

Table 1. Area matching results of SGAD on ScanNet1500 and MegaDepth1500. Measured in AUC (higher is better).

Method	AUC@3px $\uparrow$	AUC@5px $\uparrow$	AUC@10px $\uparrow$
SP[8]+SG[27] CVPR'19	53.9	68.3	81.7
LoFTR [31] CVPR'21	65.9	75.6	84.6
3DG-STFM [21] ECCV'22	64.7	73.1	81.0
AspanFormer [5] ECCV'22	67.4	76.9	85.6
TopicFM [12] AAAI'23	67.3	77.0	85.7
PDCNet+ [33] PAMI'23	67.7	77.6	86.3
DKM [10] CVPR'23	71.3	80.6	88.5
SGAD+DKM	72.1	81.3	89.2

Table 2. Homography estimation results on HPatches. Measured in AUC (higher is better).

### 4.3. Homography Estimation

We evaluate SGAD on the HPatches dataset for homography estimation, a standard benchmark containing diverse viewpoint changes and illumination variations. Following [27] and [31], we report AUC at three thresholds (3, 5, and 10 pixels), with all images pre-processed by resizing their shorter side to 480. We compare against recent approaches [5, 8, 10, 12, 21, 27, 31, 33].

**Results.** As shown in Tab. 2, SGAD significantly improves upon the strong DKM baseline, increasing AUC@3px from 71.3% to 72.1%. Unlike MESA and DMESA, which fail to establish area matches in certain scenes and are therefore excluded from comparison, SGAD maintains robust performance across all test cases. This demonstrates the superior ability of our method to handle challenging matching scenarios where previous area-based approaches typically struggle.

### 4.4. Relative Pose Estimation

**Datasets.** We assess SGAD pose estimation accuracy on ScanNet1500, a challenging indoor dataset with untextured surfaces and viewpoint variations, and on MegaDepth1500, a benchmark of 1500 outdoor image pairs.

**Experimental setup.** We conduct extensive experiments across various image resolutions. For ScanNet, we resize full images to  $1296 \times 968$  (original resolution),  $880 \times 640$ , and  $640 \times 480$ . For MegaDepth, we test at resolutions of  $1200 \times 1200$ ,  $832 \times 832$ , and  $640 \times 640$  for full images. For all experiments, cropped areas are consistently resized to  $640 \times 480$  (ScanNet) or  $640 \times 640$  (MegaDepth). Following [38], we implement MAGSAC++[1] for outlier rejection. We evaluate the performance improvement of SGAD with various point matchers and compare it against recent approaches [8, 10–13, 27, 31, 38, 39]. We evaluate pose estimation using AUC at thresholds ( $5^\circ$ ,  $10^\circ$ ,  $20^\circ$ )[27]. To assess cross-domain generalization capability, we conduct two additional experiments: testing SGAD on ScanNet using a model trained on MegaDepth (outdoor $\rightarrow$ indoor transfer), and testing on MegaDepth using a model trained on ScanNet (indoor $\rightarrow$ outdoor transfer). In both cases, we maintain point matching models trained on their respective test domains.

**Results.** Tabs. 3 and 4 demonstrate that SGAD substantially enhances the performance of all baseline methods across all resolutions for both indoor and outdoor scenes. Notably, in indoor scenes (ScanNet), at  $1296 \times 968$  resolution, SGAD achieves a +233.22% improvement in AUC@ $5^\circ$  for LoFTR, effectively addressing the matching difficulties in high-resolution indoor scenes. Moreover, compared to other methods based on the A2PM framework such as MESA and DMESA, SGAD achieves superior improvement, e.g., +30.92% in AUC@ $5^\circ$  for DKM at  $1296 \times 968$  resolution, outperforming both MESA (24.46%) and DMESA (19.58%). Additionally, in cross-domain generalization experiments for both indoor and outdoor scenes, SGAD achieves performance comparable to models trained on the test domain. Furthermore, as shown in Fig. 5, SGAD achieves more correct matches and lower rotation and translation errors on untextured scenes and with large viewpoint changes. These results demonstrate that SGAD effectively enhances the performance of various point matchers while exhibiting strong generalization ability and robustness. Significantly, when combined with the SOTA method ROMA, SGAD provides significant improvement across all resolutions in both indoor and outdoor scenes, with SGAD+ROMA establishing a new *state-of-the-art*.

Pose estimation AUC	ScanNet1500 benchmark								
	1296 × 968			880 × 640			640 × 480		
	AUC@5° ↑	AUC@10° ↑	AUC@20° ↑	AUC@5° ↑	AUC@10° ↑	AUC@20° ↑	AUC@5° ↑	AUC@10° ↑	AUC@20° ↑
TopicFM [12] AAI'23	19.14	36.55	52.68	19.23	36.48	52.49	19.45	36.57	52.75
TopicFM+ [13] TIP'24	20.26	37.83	54.06	19.73	37.19	53.64	20.00	37.79	53.98
SP[8]+SG[27] CVPR'19	22.62	42.89	61.44	23.37	43.68	62.76	21.73	41.64	60.41
SGAD+SPSG	25.74 <sub>+13.79%</sub>	45.95 <sub>+7.13%</sub>	63.77 <sub>+3.79%</sub>	25.17 <sub>+7.70%</sub>	45.46 <sub>+4.08%</sub>	63.48 <sub>+1.15%</sub>	24.31 <sub>+11.87%</sub>	44.64 <sub>+7.20%</sub>	62.92 <sub>+4.15%</sub>
LoFTR [31] CVPR'21	8.91	18.31	29.56	20.01	39.50	57.70	28.44	50.43	68.80
SGAD+LoFTR	29.69 <sub>+233.22%</sub>	51.50 <sub>+181.27%</sub>	69.58 <sub>+135.39%</sub>	28.79 <sub>+43.88%</sub>	50.68 <sub>+28.30%</sub>	68.92 <sub>+19.45%</sub>	28.69 <sub>+0.88%</sub>	51.18 <sub>+1.49%</sub>	69.40 <sub>+0.87%</sub>
DKM [10] CVPR'23	24.16	44.03	61.34	29.30	51.02	68.51	30.17	51.80	69.52
MESA [39]+DKM CVPR'24	30.07 <sub>+24.46%</sub>	51.57 <sub>+17.12%</sub>	68.98 <sub>+12.46%</sub>	30.76 <sub>+4.98%</sub>	52.59 <sub>+3.08%</sub>	69.74 <sub>+1.80%</sub>	30.85 <sub>+2.25%</sub>	52.57 <sub>+1.49%</sub>	69.97 <sub>+0.65%</sub>
DMESA [38]+DKM Arxiv'24	28.89 <sub>+19.58%</sub>	49.34 <sub>+12.06%</sub>	66.28 <sub>+8.05%</sub>	30.61 <sub>+4.47%</sub>	51.95 <sub>+1.82%</sub>	69.14 <sub>+0.92%</sub>	30.90 <sub>+2.42%</sub>	52.31 <sub>+0.98%</sub>	69.86 <sub>+0.49%</sub>
SGAD+DKM	31.63 <sub>+30.92%</sub>	52.98 <sub>+20.33%</sub>	69.93 <sub>+14.00%</sub>	31.85 <sub>+8.70%</sub>	53.11 <sub>+4.10%</sub>	70.12 <sub>+2.35%</sub>	31.65 <sub>+4.91%</sub>	53.12 <sub>+2.55%</sub>	70.69 <sub>+1.68%</sub>
SGAD <sup>†</sup> +DKM	31.51 <sub>+30.42%</sub>	52.87 <sub>+20.08%</sub>	69.87 <sub>+13.91%</sub>	31.76 <sub>+8.40%</sub>	53.02 <sub>+3.92%</sub>	70.05 <sub>+2.25%</sub>	31.49 <sub>+4.38%</sub>	52.92 <sub>+2.16%</sub>	70.55 <sub>+1.48%</sub>
ROMA [11] CVPR'24	31.51	53.44	71.10	31.99	53.90	71.39	31.80	53.92	71.29
SGAD+ROMA	<b>33.84</b> <sub>+7.39%</sub>	<b>55.37</b> <sub>+3.61%</sub>	<b>72.23</b> <sub>+1.59%</sub>	<b>33.61</b> <sub>+5.06%</sub>	<b>55.19</b> <sub>+2.39%</sub>	<b>72.11</b> <sub>+1.01%</sub>	<b>33.49</b> <sub>+5.31%</sub>	<b>55.14</b> <sub>+2.26%</sub>	<b>72.16</b> <sub>+1.22%</sub>

Table 3. Relative pose estimation results (%) on ScanNet1500. Measured in AUC (higher is better). <sup>†</sup> denotes model trained on the MegaDepth dataset.

Pose estimation AUC	MegaDepth1500 benchmark								
	1200 × 1200			832 × 832			640 × 640		
	AUC@5° ↑	AUC@10° ↑	AUC@20° ↑	AUC@5° ↑	AUC@10° ↑	AUC@20° ↑	AUC@5° ↑	AUC@10° ↑	AUC@20° ↑
SP[8]+SG[27] CVPR'19	56.83	71.9	83.03	53.32	68.75	80.66	47.28	63.57	76.50
TopicFM [12] AAI'23	52.68	69.44	81.42	49.36	67.28	80.01	46.53	64.15	77.73
TopicFM+ [13] TIP'24	56.52	71.93	82.87	55.03	70.18	81.49	49.53	65.31	77.49
LoFTR [31] CVPR'21	62.37	76.34	85.96	60.64	74.82	84.83	56.42	71.80	82.65
SGAD+LoFTR	65.98 <sub>+5.79%</sub>	78.77 <sub>+3.18%</sub>	87.13 <sub>+1.36%</sub>	65.16 <sub>+7.45%</sub>	77.94 <sub>+4.17%</sub>	86.62 <sub>+2.11%</sub>	63.94 <sub>+13.33%</sub>	76.90 <sub>+7.10%</sub>	85.78 <sub>+3.79%</sub>
DKM [10] CVPR'23	61.11	74.63	84.02	62.42	75.88	85.11	63.26	76.13	84.97
MESA [39]+DKM CVPR'24	62.31 <sub>+1.96%</sub>	76.11 <sub>+1.98%</sub>	85.56 <sub>+1.83%</sub>	62.68 <sub>+0.42%</sub>	75.96 <sub>+0.11%</sub>	85.35 <sub>+0.28%</sub>	63.02 <sub>-0.38%</sub>	76.31 <sub>+0.24%</sub>	85.60 <sub>+0.74%</sub>
DMESA [38]+DKM Arxiv'24	63.52 <sub>+3.94%</sub>	76.29 <sub>+2.22%</sub>	85.31 <sub>+1.54%</sub>	64.02 <sub>+2.56%</sub>	76.69 <sub>+1.07%</sub>	85.54 <sub>+0.51%</sub>	65.24 <sub>+3.13%</sub>	77.98 <sub>+2.43%</sub>	86.55 <sub>+1.86%</sub>
SGAD+DKM	66.40 <sub>+8.66%</sub>	78.38 <sub>+5.02%</sub>	86.51 <sub>+2.96%</sub>	66.49 <sub>+6.52%</sub>	78.80 <sub>+3.85%</sub>	87.23 <sub>+2.49%</sub>	66.75 <sub>+5.52%</sub>	78.80 <sub>+3.51%</sub>	87.13 <sub>+2.54%</sub>
SGAD <sup>†</sup> +DKM	66.04 <sub>+8.08%</sub>	78.07 <sub>+4.61%</sub>	86.50 <sub>+2.95%</sub>	65.97 <sub>+5.69%</sub>	78.35 <sub>+3.26%</sub>	86.88 <sub>+2.08%</sub>	66.73 <sub>+5.49%</sub>	78.39 <sub>+2.97%</sub>	86.67 <sub>+2.00%</sub>
ROMA [11] CVPR'24	65.68	78.15	86.68	65.91	78.41	86.95	65.29	78.01	86.68
SGAD+ROMA	<b>67.85</b> <sub>+3.30%</sub>	<b>79.87</b> <sub>+2.20%</sub>	<b>88.02</b> <sub>+1.55%</sub>	<b>68.34</b> <sub>+3.69%</sub>	<b>80.27</b> <sub>+2.37%</sub>	<b>88.34</b> <sub>+1.57%</sub>	<b>67.94</b> <sub>+4.06%</sub>	<b>80.09</b> <sub>+2.67%</sub>	<b>88.40</b> <sub>+1.98%</sub>

Table 4. Relative pose estimation results (%) on MegaDepth1500. Measured in AUC (higher is better). <sup>†</sup> denotes model trained on the ScanNet dataset.

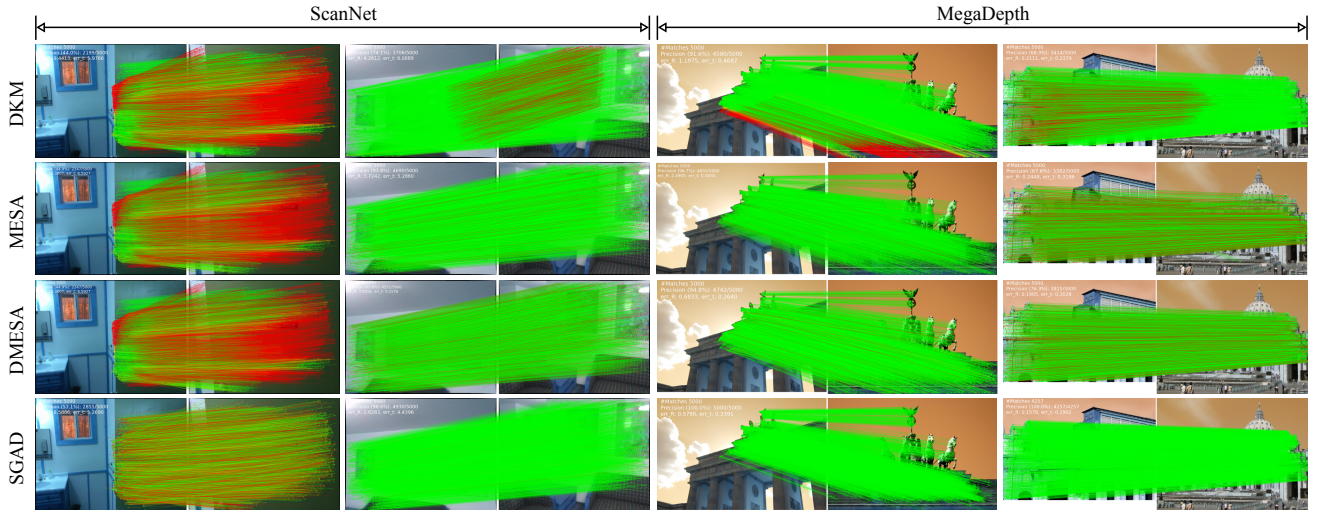


Figure 5. Qualitative comparison. We compare SGAD against MESA [39] and DMESA [38], with all three methods using DKM [10] as the downstream point matcher. SGAD achieves more correct matches and lower rotation and translation errors on scenes with large viewpoint changes (MegaDepth) and untextured scenes (ScanNet).

#### 4.5. Runtime

We conducted comprehensive timing experiments on both indoor and outdoor datasets to evaluate computational efficiency, with an RTX A6000 GPU. For all methods tested, images from the MegaDepth dataset were resized to  $1200 \times 1200$  pixels, while images from the ScanNet dataset retained their original dimensions ( $1296 \times 968$  pixels). The area size was consistently resized to  $480 \times 480$  pixels. The SAM extraction step is offline, so we do not include it in the timing.

**Results.** As shown in Tab. 5, SGAD demonstrated significant computational efficiency improvements in both indoor and outdoor scenes compared to previous A2PM methods. The processing times on MegaDepth of  $0.82s$  for SGAD+LoFTR versus  $60.23s$  for MESA+LoFTR and  $1.84s$  for DMESA+LoFTR. Furthermore, our analysis in Tabs. 4 and 5 reveals that SGAD+LoFTR (semi-dense) not only achieved lower processing times than DKM (dense) ( $0.82s$  *vs.*  $1.51s$ ) but also consistently outperformed it across multiple resolution levels, delivering superior accuracy with AUC@5° values of  $65.98$  *vs.*  $61.11$  at  $1200 \times 1200$  resolution and  $65.16$  *vs.*  $62.42$  at  $832 \times 832$  resolution, thereby demonstrating that our approach provides both computational efficiency and performance advantages in diverse scenarios.

#### 4.6. Ablation Study

We perform ablation studies on ScanNet to validate our design choices (Tab. 6). 1) The DINOv2-only baseline achieves  $79.74$  AUC@0.2. 2) & 3) Sequentially adding the attention mechanism and positional encoding (PE) progressively boosts performance to  $92.52$  and finally  $95.46$ , demonstrating that all architectural components are essential and the gains do not merely stem from the powerful backbone. 4) & 5) The study also highlights our supervision strategy’s effectiveness: removing the ranking loss ( $\mathcal{L}_{rank}$ ) degrades performance, while replacing our dual-task loss with a standard Triplet loss causes a significant drop to  $91.81$  AUC. This confirms the superiority of our proposed framework.

We analyze the sensitivity of our HCRF parameters on a randomly sampled subset of 300 image pairs. As shown in Fig. 6, we achieve the best AUC@5° gains of  $+6.79$  at  $(0.4, 0.9)$  on MegaDepth and  $+7.65$  at  $(0.4, 0.85)$  on ScanNet. Parameters within the ranges of Coverage=[0.4-0.5] and Overlap=[0.85-0.9] perform well across both datasets.

### 5. Conclusion

We introduced SGAD, a new paradigm for Area to Point Matching (A2PM). Our approach redefines the

	LoFTR	DKM	MESA+LoFTR	DMESA+LoFTR	SGAD+LoFTR
MegaDepth	0.38	1.51	60.23	1.84	0.82
ScanNet	0.28	0.72	33.44	1.38	0.67

Table 5. Runtime Comparison on an RTX A6000 GPU (seconds). SGAD includes Descriptor Network, Descriptor Matching, and HCRF.

	DINOv2	Attention	PE	$\mathcal{L}_{cls}$	$\mathcal{L}_{rank}$	$\mathcal{L}_{Triplet}$	AUC @0.2↑	AUC @0.3↑
1)	✓	✗	✗	✓	✓	✗	79.74	82.62
2)	✓	✓	✗	✓	✓	✗	92.52	94.23
3)	✓	✓	✓	✓	✓	✗	<b>95.46</b>	<b>96.18</b>
4)	✓	✓	✓	✓	✗	✗	94.82	95.61
5)	✓	✓	✓	✗	✗	✓	91.81	93.55

Table 6. Ablation study. Comparison of different variants of SGAD trained and evaluated on the ScanNet1500.

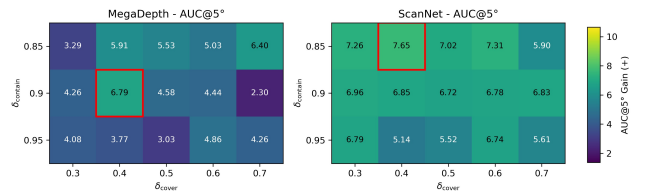


Figure 6. Sensitivity analysis of the HCRF module. The heatmaps plot the absolute AUC@5° gain of SGAD over the LoFTR baseline for pose estimation. Results are shown for MegaDepth (640x640) and ScanNet (880x640).

task by learning to generate discriminative, holistic descriptors for image areas, enabling direct and efficient matching. This circumvents the bottlenecks of traditional methods, which rely on costly dense feature comparisons or complex graph-based optimization. This synergistic design proves both robust and efficient. Extensive experiments show that SGAD not only achieves state-of-the-art accuracy but also significantly improves computational efficiency. Its robust performance gains across multiple point matchers validate its potential as a new foundational component for feature matching pipelines.

**Limitations and Future Work.** While SGAD demonstrates strong performance, certain limitations remain. First, pooling area features into compact vectors limits their expressive power in challenging cases that combine high visual similarity with extreme geometric transformations, leading to matching failures (see supplementary material). Second, despite HCRF filtering, partial overlaps can persist among the matched areas, causing redundant downstream computations. Finally, the independent training of the area matching network precludes its joint, end-to-end optimization with the point matcher. Addressing these limitations will be the focus of our future work.



## 6. Acknowledgments

This work was supported by the Natural Science Basic Research Program of Shaanxi (2024JC-YBMS-467). We thank the reviewers for their valuable feedback, as well as Guanglu Shi for his help with our experiments. We also gratefully acknowledge the authors of LoFTR [31] and MESA [39] for their open-source codebases which were instrumental to this work.

## References

- [1] Daniel Barath, Jana Noskova, Maksym Ivashechkin, and Jiri Matas. MAGSAC++, a fast, reliable and accurate robust estimator. In *Proceedings of the IEEE/CVF Conference on Computer Vision and Pattern Recognition*, pages 1304–1312, 2020. 6
- [2] Axel Barroso-Laguna, Edgar Riba, Daniel Ponsa, and Krystian Mikolajczyk. Key.Net: Keypoint detection by handcrafted and learned CNN filters. In *Proceedings of the IEEE/CVF International Conference on Computer Vision*, pages 5836–5844, 2019. 2
- [3] Carlos Campos, Richard Elvira, Juan J Gómez Rodríguez, José MM Montiel, and Juan D Tardós. ORB-SLAM3: An accurate open-source library for visual, visual-inertial, and multimap SLAM. *IEEE Transactions on Robotics*, 37(6):1874–1890, 2021. 1
- [4] Zhe Cao, Tao Qin, Tie-Yan Liu, Ming-Feng Tsai, and Hang Li. Learning to rank: from pairwise approach to listwise approach. In *Proceedings of the International Conference on Machine Learning*, pages 129–136, 2007. 5
- [5] Hongkai Chen, Zixin Luo, Lei Zhou, Yurun Tian, Mingmin Zhen, Tian Fang, David Mckinnon, Yanghai Tsin, and Long Quan. ASpanFormer: Detector-free image matching with adaptive span transformer. In *Proceedings of the European Conference on Computer Vision*, pages 20–36. Springer, 2022. 6
- [6] Ying Chen, Dihe Huang, Shang Xu, Jianlin Liu, and Yong Liu. Guide local feature matching by overlap estimation. In *Proceedings of the AAAI Conference on Artificial Intelligence*, pages 365–373, 2022. 1
- [7] Angela Dai, Angel X Chang, Manolis Savva, Maciej Halber, Thomas Funkhouser, and Matthias Nießner. ScanNet: Richly-annotated 3D reconstructions of indoor scenes. In *Proceedings of the IEEE/CVF Conference on Computer Vision and Pattern Recognition*, pages 5828–5839, 2017. 5
- [8] Daniel DeTone, Tomasz Malisiewicz, and Andrew Rabinovich. SuperPoint: Self-supervised interest point detection and description. In *Proceedings of the IEEE/CVF Conference on Computer Vision and Pattern Recognition Workshops*, pages 224–236, 2018. 2, 6, 7
- [9] Mihai Dusmanu, Ignacio Rocco, Tomas Pajdla, Marc Pollefeys, Josef Sivic, Akihiko Torii, and Torsten Sattler. D2-Net: A trainable CNN for joint description and detection of local features. In *Proceedings of the IEEE/CVF Conference on Computer Vision and Pattern Recognition*, pages 8092–8101, 2019. 2
- [10] Johan Edstedt, Ioannis Athanasiadis, Mårten Wadenbäck, and Michael Felsberg. DKM: Dense kernelized feature matching for geometry estimation. In *Proceedings of the IEEE/CVF Conference on Computer Vision and Pattern Recognition*, pages 17765–17775, 2023. 2, 6, 7, 4
- [11] Johan Edstedt, Qiyu Sun, Georg Bökman, Mårten Wadenbäck, and Michael Felsberg. RoMa: Robust dense feature matching. In *Proceedings of the IEEE/CVF Conference on Computer Vision and Pattern Recognition*, pages 19790–19800, 2024. 7
- [12] Khang Truong Giang, Soohwan Song, and Sungho Jo. TopicFM: Robust and interpretable topic-assisted feature matching. In *Proceedings of the AAAI Conference on Artificial Intelligence*, pages 2447–2455, 2023. 1, 2, 6, 7
- [13] Khang Truong Giang, Soohwan Song, and Sungho Jo. TopicFM+: Boosting accuracy and efficiency of topic-assisted feature matching. *IEEE Transactions on Image Processing*, 2024. 6, 7
- [14] Dihe Huang, Ying Chen, Yong Liu, Jianlin Liu, Shang Xu, Wenlong Wu, Yikang Ding, Fan Tang, and Chengjie Wang. Adaptive assignment for geometry aware local feature matching. In *Proceedings of the IEEE/CVF Conference on Computer Vision and Pattern Recognition*, pages 5425–5434, 2023. 1
- [15] Alexander Kirillov, Eric Mintun, Nikhila Ravi, Hanzi Mao, Chloe Rolland, Laura Gustafson, Tete Xiao, Spencer Whitehead, Alexander C Berg, Wan-Yen Lo, et al. Segment anything. In *Proceedings of the IEEE/CVF International Conference on Computer Vision*, pages 4015–4026, 2023. 1, 2
- [16] Zhengqi Li and Noah Snavely. MegaDepth: Learning single-view depth prediction from internet photos. In *Proceedings of the IEEE/CVF Conference on Computer Vision and Pattern Recognition*, pages 2041–2050, 2018. 5
- [17] Tsung-Yi Lin, Priya Goyal, Ross Girshick, Kaiming He, and Piotr Dollár. Focal loss for dense object detection. In *Proceedings of the IEEE/CVF International Conference on Computer Vision*, pages 2980–2988, 2017. 5
- [18] Philipp Lindenberger, Paul-Edouard Sarlin, and Marc Pollefeys. LightGlue: Local feature matching at light speed. In *Proceedings of the IEEE/CVF International Conference on Computer Vision*, pages 17627–17638, 2023. 2
- [19] Ilya Loshchilov and Frank Hutter. Decoupled weight decay regularization. In *Proceedings of the International Conference on Learning Representations*, 2019. 5
- [20] David G Lowe. Distinctive image features from scale-invariant keypoints. *International Journal of Computer Vision*, 60(2):91–110, 2004. 2
- [21] Runyu Mao, Chen Bai, Yatong An, Fengqing Zhu, and Cheng Lu. 3DG-STFM: 3D geometric guided student-

- teacher feature matching. In *Proceedings of the European Conference on Computer Vision*, pages 125–142. Springer, 2022. 6
- [22] Junjie Ni, Yijin Li, Zhaoyang Huang, Hongsheng Li, Hujun Bao, Zhaopeng Cui, and Guofeng Zhang. PATS: Patch area transportation with subdivision for local feature matching. In *Proceedings of the IEEE/CVF Conference on Computer Vision and Pattern Recognition*, pages 17776–17786, 2023. 2
- [23] Maxime Oquab, Timothée Darcet, Théo Moutakanni, Huy Vo, Marc Szafraniec, Vasil Khalidov, Pierre Fernandez, Daniel Haziza, Francisco Massa, Alaaeldin El-Nouby, et al. DINOv2: Learning robust visual features without supervision. *Transactions on Machine Learning Research*, 2024. 2, 5
- [24] Filip Radenović, Giorgos Tolias, and Ondřej Chum. Fine-tuning CNN image retrieval with no human annotation. *IEEE Transactions on Pattern Analysis and Machine Intelligence*, 41(7):1655–1668, 2018. 1
- [25] Jerome Revaud, Cesar De Souza, Martin Humenberger, and Philippe Weinzaepfel. R2D2: Repeatable and reliable detector and descriptor. *Advances in Neural Information Processing Systems*, 32:12405–12415, 2019. 2
- [26] Ignacio Rocco, Mircea Cimpoi, Relja Arandjelović, Akihiko Torii, Tomas Pajdla, and Josef Sivic. Neighbourhood consensus networks. *Advances in Neural Information Processing Systems*, 31, 2018. 4
- [27] Paul-Edouard Sarlin, Daniel DeTone, Tomasz Malisiewicz, and Andrew Rabinovich. SuperGlue: Learning feature matching with graph neural networks. In *Proceedings of the IEEE/CVF Conference on Computer Vision and Pattern Recognition*, pages 4938–4947, 2020. 2, 5, 6, 7
- [28] Paul-Edouard Sarlin, Ajaykumar Unagar, Mans Larsson, Hugo Germain, Carl Toft, Viktor Larsson, Marc Pollefeys, Vincent Lepetit, Lars Hammarstrand, Fredrik Kahl, et al. Back to the feature: Learning robust camera localization from pixels to pose. In *Proceedings of the IEEE/CVF Conference on Computer Vision and Pattern Recognition*, pages 3247–3257, 2021. 1
- [29] Torsten Sattler, Akihiko Torii, Josef Sivic, Marc Pollefeys, Hajime Taira, Masatoshi Okutomi, and Tomas Pajdla. Are large-scale 3D models really necessary for accurate visual localization? In *Proceedings of the IEEE/CVF Conference on Computer Vision and Pattern Recognition*, pages 1637–1646, 2017. 1
- [30] Johannes L Schonberger and Jan-Michael Frahm. Structure-From-Motion revisited. In *Proceedings of the IEEE/CVF Conference on Computer Vision and Pattern Recognition*, pages 4104–4113, 2016. 1
- [31] Jiaming Sun, Zehong Shen, Yuang Wang, Hujun Bao, and Xiaowei Zhou. LoFTR: Detector-free local feature matching with transformers. In *Proceedings of the IEEE/CVF Conference on Computer Vision and Pattern Recognition*, pages 8922–8931, 2021. 2, 5, 6, 7, 9
- [32] Robert Tarjan. Depth-First Search and linear graph algorithms. *SIAM Journal on Computing*, 1(2):146–160, 1972. 4
- [33] Prune Truong, Martin Danelljan, Radu Timofte, and Luc Van Gool. PDC-Net+: Enhanced probabilistic dense correspondence network. *IEEE Transactions on Pattern Analysis and Machine Intelligence*, 45(8):10247–10266, 2023. 6
- [34] Michał Tyszkiewicz, Pascal Fua, and Eduard Trulls. DISK: Learning local features with policy gradient. *Advances in Neural Information Processing Systems*, 33:14254–14265, 2020. 4
- [35] Ashish Vaswani, Noam Shazeer, Niki Parmar, Jakob Uszkoreit, Llion Jones, Aidan N Gomez, Łukasz Kaiser, and Illia Polosukhin. Attention is all you need. *Advances in Neural Information Processing Systems*, 30, 2017. 2
- [36] Jiahui Yu, Yuning Jiang, Zhangyang Wang, Zhimin Cao, and Thomas Huang. UnitBox: An advanced object detection network. In *Proceedings of the ACM International Conference on Multimedia*, pages 516–520, 2016. 5
- [37] Jiahui Zhang, Dawei Sun, Zixin Luo, Anbang Yao, Lei Zhou, Tianwei Shen, Yurong Chen, Long Quan, and Hongen Liao. Learning two-view correspondences and geometry using order-aware network. In *Proceedings of the IEEE/CVF International Conference on Computer Vision*, pages 5845–5854, 2019. 2
- [38] Yesheng Zhang and Xu Zhao. DMESA: Densely matching everything by segmenting anything. *arXiv preprint arXiv:2408.00279*, 2024. 2, 6, 7, 3, 4
- [39] Yesheng Zhang and Xu Zhao. MESA: Matching everything by segmenting anything. In *Proceedings of the IEEE/CVF Conference on Computer Vision and Pattern Recognition*, pages 20217–20226, 2024. 1, 2, 6, 7, 9, 3, 4
- [40] Yesheng Zhang, Xu Zhao, and Dahong Qian. Searching from area to point: A hierarchical framework for semantic-geometric combined feature matching. *arXiv preprint arXiv:2305.00194*, 2023. 1, 2
- [41] Qunjie Zhou, Torsten Sattler, and Laura Leal-Taixe. Patch2Pix: Epipolar-guided pixel-level correspondences. In *Proceedings of the IEEE/CVF Conference on Computer Vision and Pattern Recognition*, pages 4669–4678, 2021. 2

# SGAD: Semantic and Geometric-aware Descriptor for Local Feature Matching

## Supplementary Material

### A. Time Complexity Analysis

This section investigates the computational complexity of MESA [39] and SGAD. Given source and target images containing  $M$  and  $N$  areas, respectively, with each area resized to  $H \times W$  pixels, our analysis focuses on the similarity computation stage.

#### A.1. MESA

MESA formulates area matching as a graph matching problem, where each area in the source and target images is represented as a graph node. In the first stage, activity maps are computed by applying self-attention and cross-attention on feature maps that have been downsampled to  $\frac{1}{8}$  of the original resolution. The similarity of each paired area ( $R_A^i, R_B^j$ ) is then determined as the product of their activity map expectations. The complexity is:

$$\mathcal{O}(L \times M \times N \times ((H' \times W')^2 \times D)), \quad (15)$$

where  $H' = \frac{H}{8}$ ,  $W' = \frac{W}{8}$ ,  $L$  is the number of attention layers, and  $D$  is the feature dimension.

To reduce this complexity, MESA employs Area Bayesian Network optimization to filter areas, reducing the number of areas to  $M'$  and  $N'$ . The complexity becomes:

$$\mathcal{O}(L \times M' \times N' \times ((H' \times W')^2 \times D)), \quad (16)$$

where  $M' < M$  and  $N' < N$ .

The subsequent graph matching has a computational complexity of:

$$\mathcal{O}(M^2 + N^2). \quad (17)$$

#### A.2. SGAD

SGAD adopts a distinct strategy. For each area, it generates a compact descriptor by first pooling the corresponding DINOv2 features into a single vector. This initial descriptor is subsequently refined through  $N_{tr}$  layers of self-attention and cross-attention. The computational complexity is:

$$\mathcal{O}(N_{tr} \times M \times N \times D), \quad (18)$$

where  $D$  represents the feature dimension, which is independent of the image resolution.

Method	Step	Complexity
MESA [39]	Similarity Calculation	$\mathcal{O}(L \times M' \times N' \times (H' \times W')^2 \times D)$
	Graph Matching	$\mathcal{O}(M^2 + N^2)$
	Main Bottleneck	$\mathcal{O}(L \times M' \times N' \times (H' \times W')^2 \times D)$
SGAD	Similarity Calculation	$\mathcal{O}(N_{tr} \times M \times N \times D)$
	Descriptor Matching	$\mathcal{O}(M \times N)$
	Main Bottleneck	$\mathcal{O}(N_{tr} \times M \times N \times D)$

Table 7. Complexity analysis of SGAD and MESA [39].

After generating the confidence matrix  $\mathcal{P}_{pr}$ , SGAD uses the MNN algorithm to compute the matching results. The complexity is:

$$\mathcal{O}(M \times N). \quad (19)$$

#### A.3. Comparative Analysis

As shown in Tab. 7, the primary computational complexity of both SGAD and MESA lies in the similarity calculation module. MESA computes similarity node by node, requiring a complexity as described in Eq. (16), where the pixel-based activity map computation limits parallelism, and the cost remains tied to high-resolution image features. In contrast, SGAD’s approach is independent of image resolution, which not only lowers the theoretical complexity but also enables more efficient hardware implementation, as discussed next.

In the matching stage, SGAD utilizes the Mutual Nearest Neighbor (MNN) algorithm, which operates directly on the dense confidence matrix  $\mathcal{P}_{pr}$ . The MNN algorithm benefits from efficient GPU parallelization due to its simplicity and the dense matrix structure, making it highly scalable for large-scale tasks. By contrast, the graph matching in MESA relies on iterative optimizations over sparsely connected graphs, which inherently limits its scalability and efficiency, especially when dealing with a large number of areas.

To validate the theoretical analysis, we measured the runtime performance of MESA and SGAD under varying numbers of areas (AreaNum). As shown in Tab. 8, the empirical results closely align with the theoretical predictions. When AreaNum increases from 11.18 to 30.89, the runtime of MESA increases by more than 6 times (from 49.92s to 311.63s). In contrast, when AreaNum increases from 15.13 to 36.44, SGAD exhibits only a minor runtime increase of approximately 36%

Method	Time(s)↓	AreaNum	AreaMatchesNum
MESA [39]	49.92	11.18	7.42
SGAD	<b>0.25</b>	15.13	10.44
MESA [39]	311.63	30.89	19.91
SGAD	<b>0.34</b>	36.44	21.54

Table 8. Runtime comparison for the area matching stage on the MegaDepth1500 benchmark. The results highlight the superior efficiency of SGAD compared to MESA [39].

Pose AUC	MegaDepth1500 benchmark(image size 1200x1200)								
	832x832 (area size)			640x640 (area size)			480x480 (area size)		
	@5° ↑	@10° ↑	@20° ↑	@5° ↑	@10° ↑	@20° ↑	@5° ↑	@10° ↑	@20° ↑
LoFTR	61.49	75.47	85.27	61.49	75.47	85.27	61.49	75.47	85.27
SGAD+LoFTR	<b>66.24</b>	<b>78.40</b>	<b>86.75</b>	<b>65.10</b>	<b>77.90</b>	<b>86.44</b>	<b>65.12</b>	<b>77.86</b>	<b>86.56</b>
DKM	61.11	74.63	84.02	61.11	74.63	84.02	61.11	74.63	84.02
SGAD+DKM	<b>66.40</b>	<b>78.38</b>	<b>86.51</b>	<b>65.97</b>	<b>78.02</b>	<b>86.38</b>	<b>65.91</b>	<b>78.27</b>	<b>86.52</b>
ROMA	65.68	78.15	86.68	65.68	78.15	86.68	65.68	78.15	86.68
SGAD+ROMA	<b>68.43</b>	<b>80.35</b>	<b>88.26</b>	<b>68.12</b>	<b>80.24</b>	<b>88.14</b>	<b>67.17</b>	<b>79.07</b>	<b>87.32</b>

Table 9. Relative pose estimation results (%) on MegaDepth1500. Measured in AUC (higher is better). The baseline methods (LoFTR, DKM, ROMA) were evaluated on the full-resolution images, and their results are presented across all columns for direct comparison.

(from 0.25s to 0.34s), demonstrating its scalability and computational efficiency in handling large-scale tasks.

Ultimately, the significant performance gap observed in Tab. 8 stems from these fundamental architectural differences. The reliance of MESA on pixel-based activity maps and node-by-node matching leads to significant bottlenecks, particularly in high-density scenarios. By contrast, the area descriptor approach and dense matrix computations employed by SGAD drastically reduce complexity. Its ability to fully exploit GPU parallelization underscores its efficiency and suitability for large-scale tasks.

## B. Effect of Area Size on Different Point Matchers

In this section, we analyze the impact of different area sizes on the performance of various point matchers on the MegaDepth1500 benchmark. Image size resized to  $1200 \times 1200$ . For the area sizes, we tested  $832 \times 832$ ,  $640 \times 640$ , and  $480 \times 480$ . As shown in Tab. 9, SGAD significantly improves the performance of LoFTR, DKM, and Roma across multiple area sizes. This further demonstrates the effectiveness of SGAD in improving the performance of different point matchers.

## C. Failure Cases

In Fig. 7, we illustrate SGAD’s primary failure mode, which arises in challenging cases that combine high

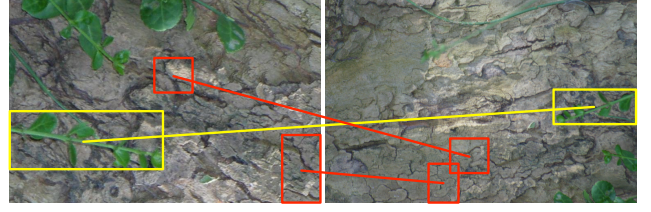


Figure 7. Failure cases of SGAD, demonstrating its vulnerability in challenging cases that combine high visual similarity and extreme geometric transformations. Mismatched areas are shown in red, correct matches in yellow.

visual similarity with extreme geometric transformations. The red color indicates mismatched areas, while the yellow color highlights correctly matched ones.

This failure stems from a detrimental synergy between our model’s architecture and its training data. Our architecture, prioritizing global context via DINOV2 and pooling, inherently sacrifices the fine-grained local features required to distinguish between visually similar areas. This architectural limitation becomes particularly critical because the training data (MegaDepth and ScanNet) lacks sufficient examples of extreme geometric transformations. Consequently, the model is not explicitly trained to be robust against such distortions. When confronted with them, it must rely more heavily on the very local details that the architecture has already discarded, leading to inevitable matching failures.

## D. Additional Qualitative Results

### D.1. Area Matching

This section provides a qualitative comparison of area matching between SGAD, MESA [39], and DMESA [38]. As shown in Fig. 8, SGAD consistently finds more content-consistent area matches across the MegaDepth and ScanNet datasets. This improved consistency establishes a stronger foundation for subsequent pixel-level matching.

### D.2. Relative Pose Estimation

Qualitative results for relative pose estimation are presented for the MegaDepth ( Figs. 9 and 10) and ScanNet ( Figs. 11 and 12) datasets. Following the protocol of LoFTR [31], we report rotation and translation errors. Match precision is visualized by epipolar error, where red indicates errors exceeding the threshold ( $1 \times 10^{-4}$  for MegaDepth and  $5 \times 10^{-4}$  for ScanNet). Across both datasets, our method consistently achieves more correct matches and lower pose errors, highlighting its robustness and accuracy under diverse conditions.



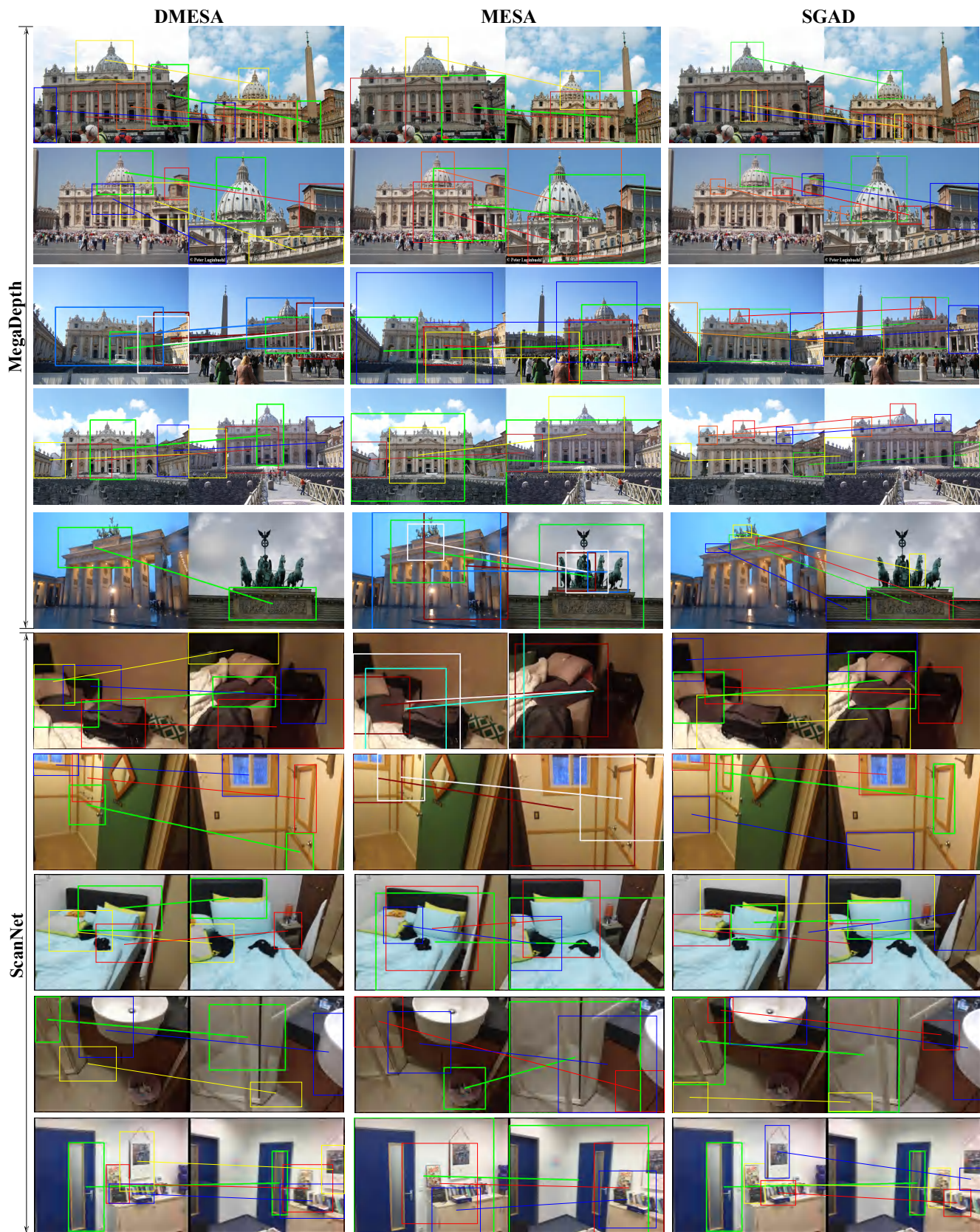


Figure 8. Qualitative comparison of area matching results on the MegaDepth and ScanNet datasets. Our method (SGAD) is compared against MESA [39] and DMESA [38]. The visualizations show that SGAD consistently identifies more semantically coherent area pairs, providing a better foundation for subsequent fine-grained matching.



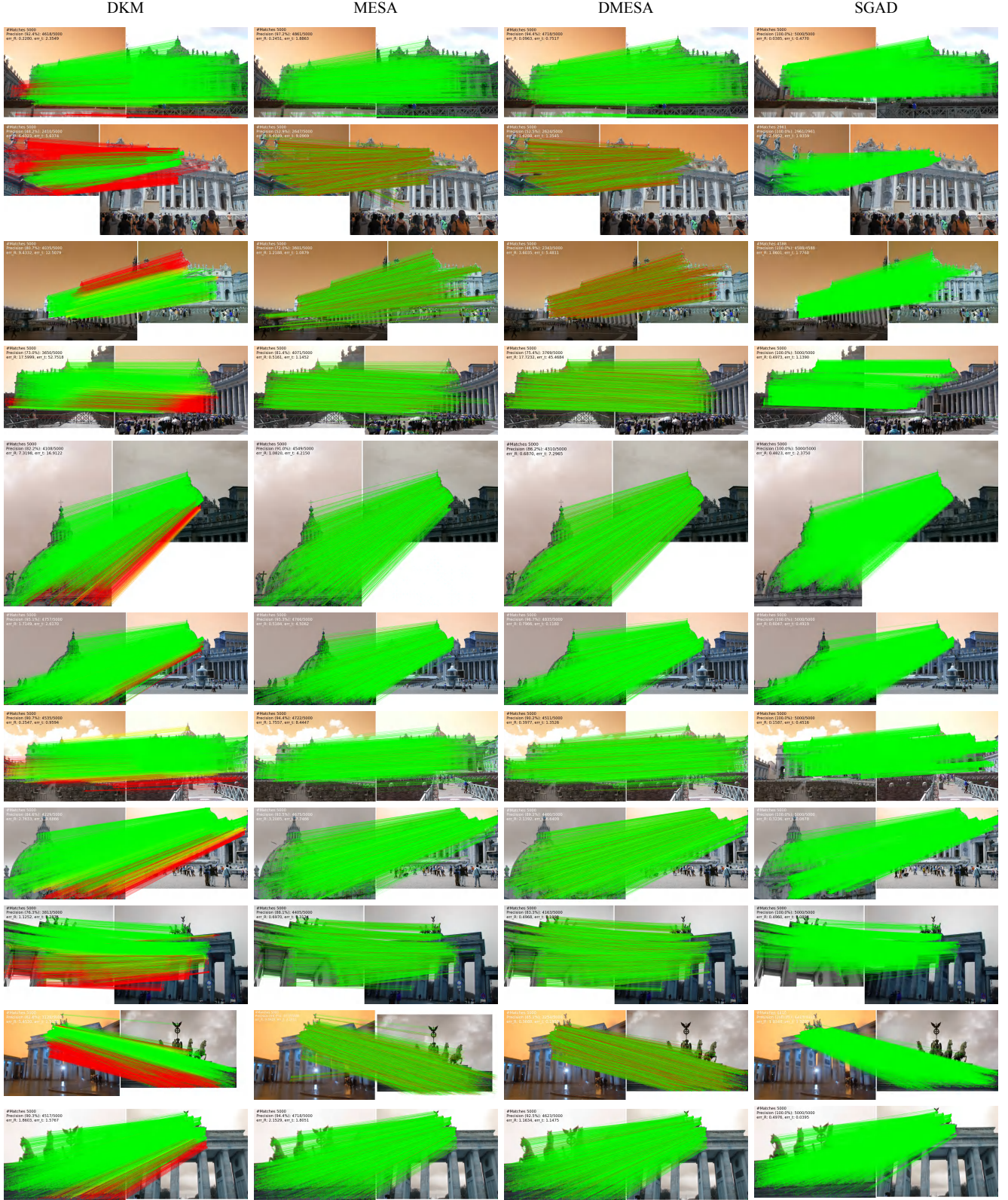


Figure 9. Qualitative comparison of matching methods on the MegaDepth dataset. Our method (SGAD) is compared against MESA [39], DMESA [38], and DKM [10]. To ensure a fair comparison of the upstream area matchers, SGAD, MESA, and DMESA all use DKM as the downstream point matcher, while DKM is also evaluated as a standalone baseline. Matches with an epipolar error greater than  $1 \times 10^{-4}$  are highlighted in red. The results show SGAD leads to more correct final matches and lower pose errors.



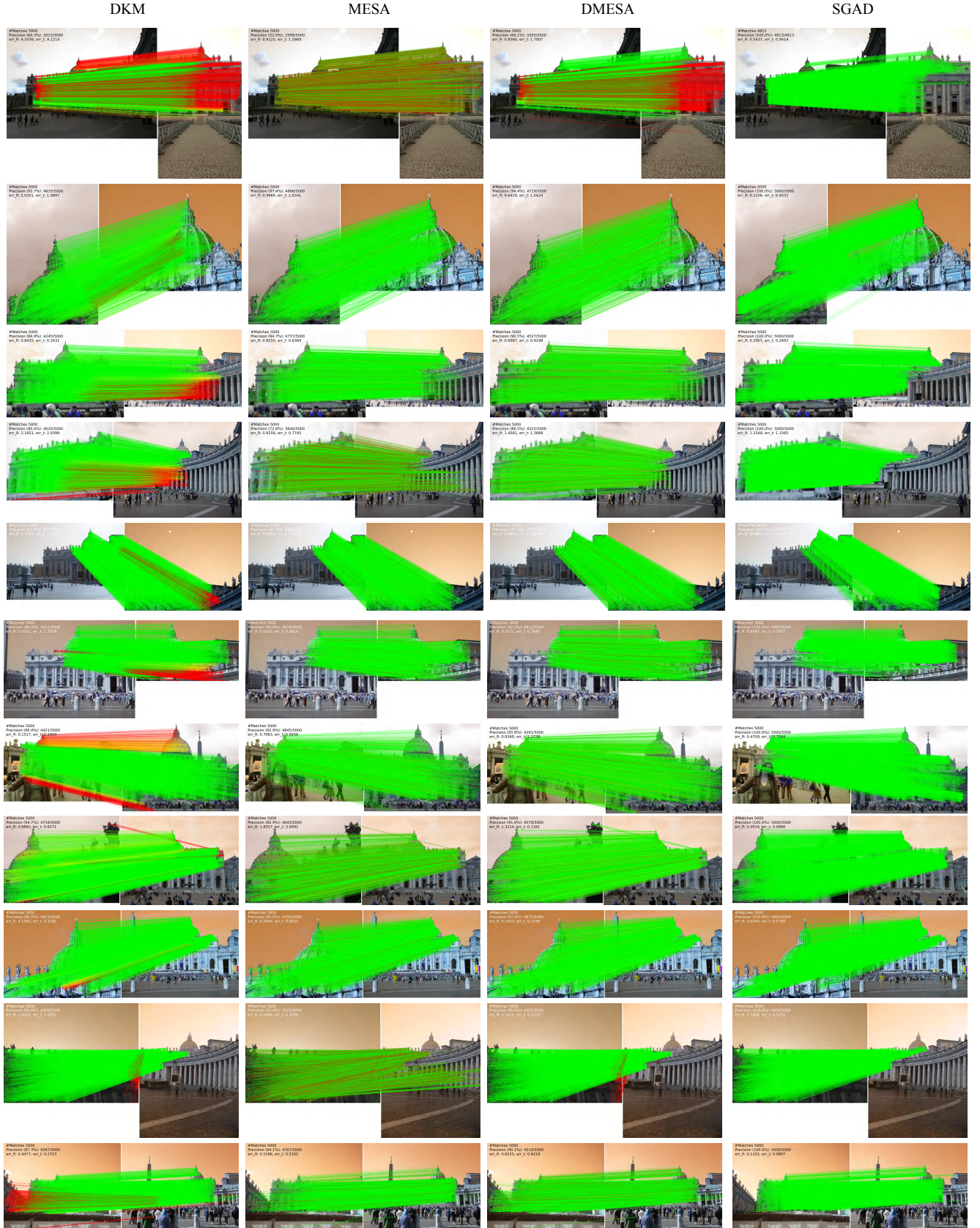


Figure 10. Qualitative comparison of matching methods on the MegaDepth dataset (continued).



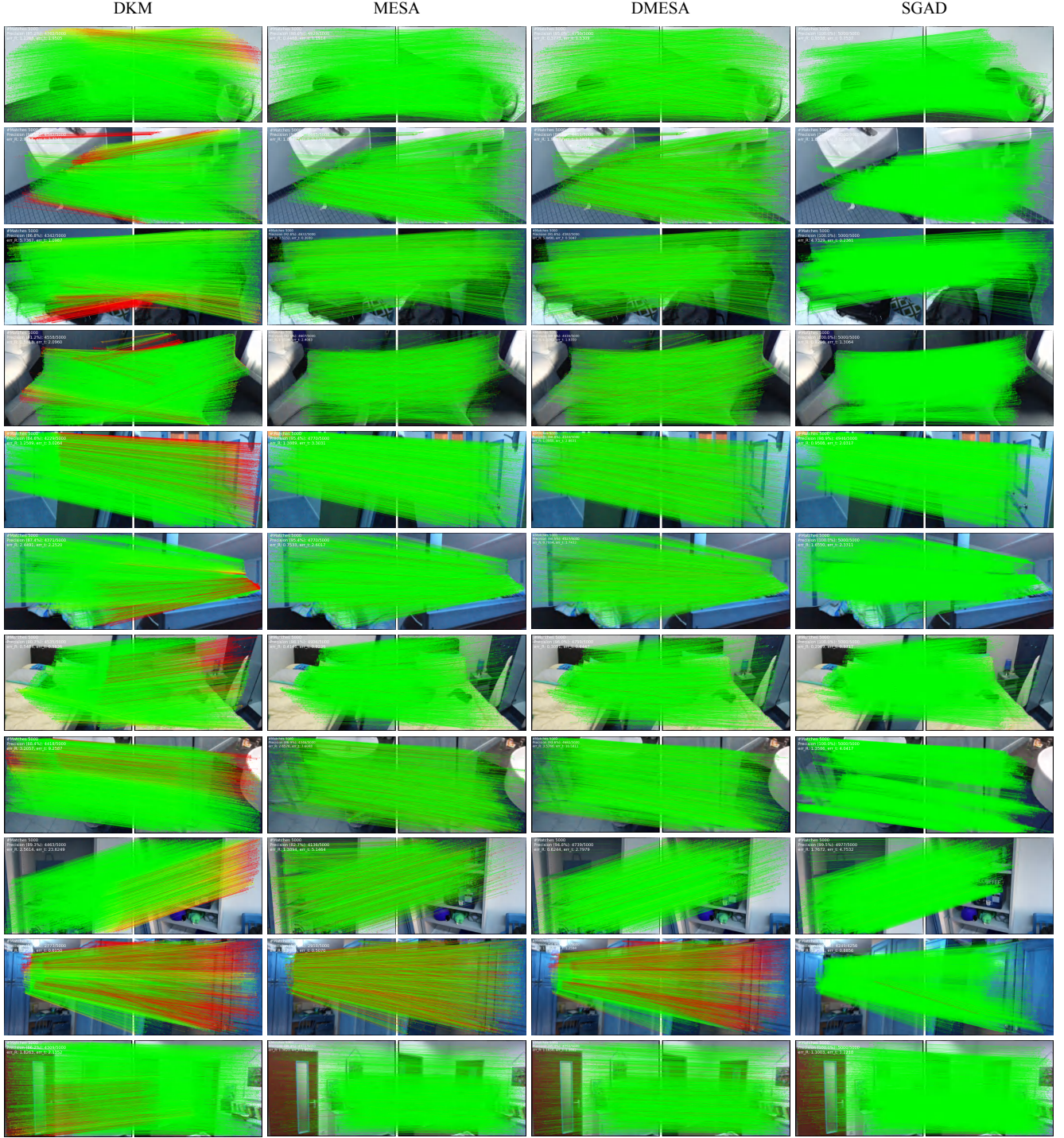


Figure 11. Qualitative comparison of matching methods on the ScanNet dataset. Our method (SGAD) is compared against MESA [39], DMESA [38], and DKM [10]. To ensure a fair comparison of the upstream area matchers, SGAD, MESA, and DMESA all use DKM as the downstream point matcher, while DKM is also evaluated as a standalone baseline. Matches with an epipolar error greater than  $5 \times 10^{-4}$  are highlighted in red. The results show SGAD leads to more correct final matches and lower pose errors.



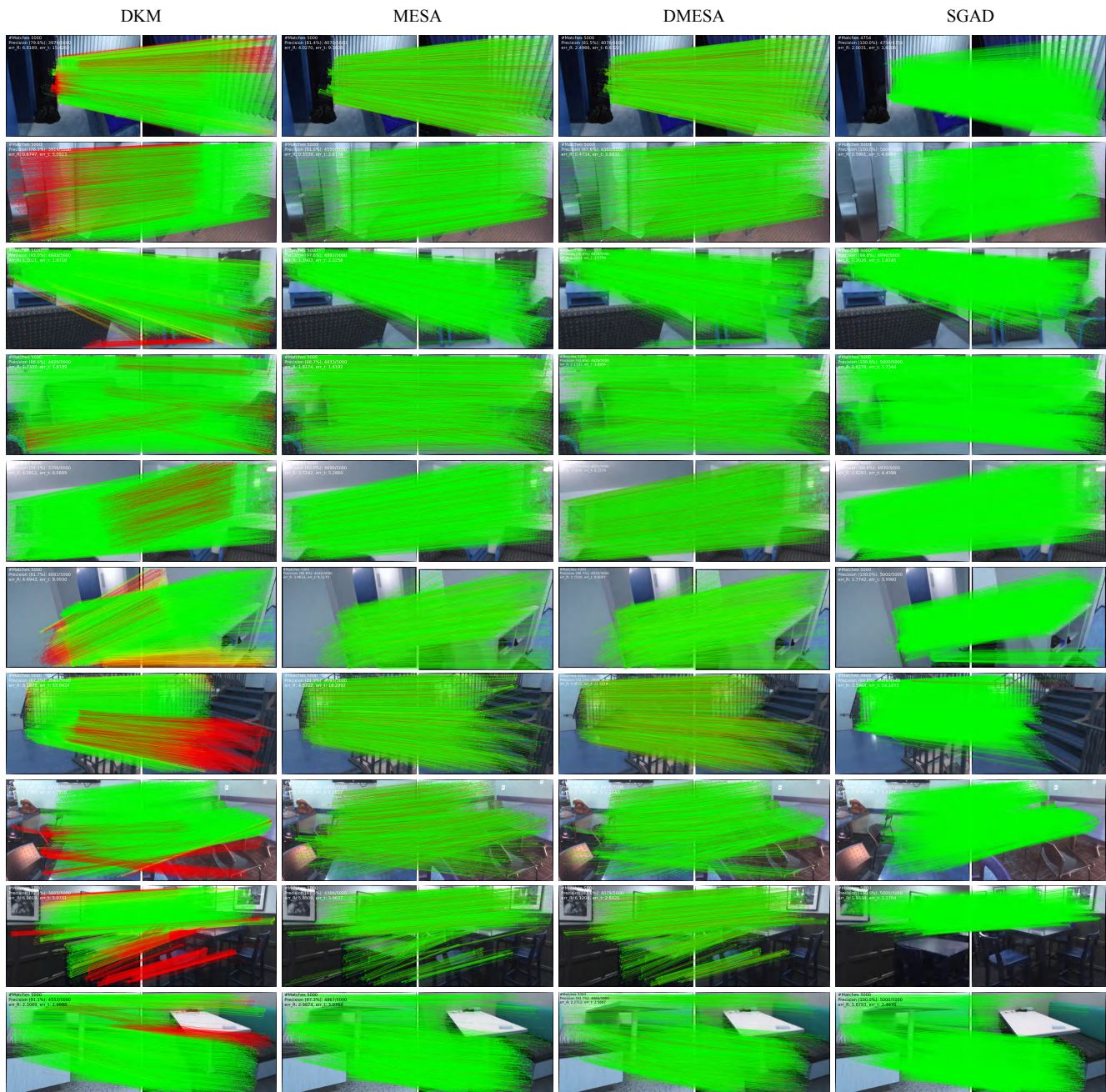


Figure 12. Qualitative comparison of matching methods on the ScanNet dataset (continued).